

# Wide 3-Dimensional Macular Ganglion Cell Complex Imaging with Spectral-Domain Optical Coherence Tomography in Glaucoma

Satoshi Morooka, Masanori Hangai, Masayuki Nukada, Noriko Nakano, Kohei Takayama, Yugo Kimura, Tadamichi Akagi, Hanako Ohashi Ikeda, Atsushi Nonaka, and Nagahisa Yoshimura

**PURPOSE.** To determine whether measurement of ganglion cell complex (GCC) thickness over a wide area (8-mm diameter) can improve the glaucoma-discriminating ability of spectral-domain optical coherence tomography (SD-OCT) compared to that in the standard macular area (6-mm diameter).

**METHODS.** Ninety-three subjects were enrolled, including 46 healthy eyes of 46 volunteers and 47 eyes of 47 glaucoma patients (23 eyes with preperimetric glaucoma [PPG] and 24 eyes with early glaucoma [EG]). All patients underwent SD-OCT raster scanning over a 9 mm × 9 mm square area centered on the fovea. Areas under the receiver operating characteristic curves (AROCs) were compared between wide sector (1–8-mm ring) and standard-size sector (1–6-mm ring) charts.

**RESULTS.** AROCs for average GCC thickness in the wide chart were significantly greater than those of the standard chart in eyes with PPG (0.928 vs. 0.891;  $P = 0.038$ ), EG (0.912 vs. 0.861;  $P = 0.003$ ), and both (0.920 vs. 0.876;  $P = 0.004$ ). Overall, the AROCs of regional GCC thicknesses were nearly comparable between the middle ring (4–6 mm) and outer ring (6–8 mm). Coefficients of variation were 0.68% and 0.97% in the standard and wide sector charts, respectively, in eyes with PPG, and 0.45% and 0.72% in the standard and wide sector charts, respectively, in eyes with EG.

**CONCLUSIONS.** Addition of the GCC thickness outside the macula to the standard macular GCC thickness significantly increased the glaucoma-discriminating ability of SD-OCT. (*Invest Ophthalmol Vis Sci.* 2012;53:4805–4812) DOI:10.1167/iovs.12-9870

Glaucomatous structural damage stems from retinal ganglion cell (RGC) loss, which is thought to be caused by damage to axons within the optic nerve head (ONH). The loss of RGC axons results in the thinning of the neuroretinal rim of the ONH and retinal nerve fiber layer (RNFL).<sup>1</sup> Damage to the RGC axons eventually causes RGC soma loss, particularly in the macula, with subsequent thinning of the ganglion cell layer (GCL).<sup>1,2</sup> Many earlier studies have determined how accurately measurements of the ONH and retinal structures can distinguish between glaucomatous and normal eyes.<sup>3–5</sup>

The development of various optical imaging technologies, such as confocal scanning laser tomography (Heidelberg Retina Tomograph, Heidelberg Engineering, Heidelberg, Germany), scanning laser polarimetry (GDx-VCC, Carl Zeiss Meditec, Dublin, CA), and optical coherence tomography (OCT; Stratus OCT, Carl Zeiss Meditec) has enabled measurement of ONH topography and circumpapillary RNFL (cpRNFL) thickness.<sup>6</sup> Among these imaging technologies, OCT has also enabled measurements of retinal thickness in the macula, which have demonstrated glaucoma-discriminating ability.<sup>7–15</sup> Advance in OCT detection technology into spectral domain (SD) combined with a broader-wavelength light source has permitted the development of SD-OCT instruments with drastically improved imaging speed and axial resolution. SD-OCT instruments allow automated measurement of the ganglion cell complex (GCC = RNFL + GCL + inner plexiform layer),<sup>16–20</sup> which more directly reflects RGC loss than retinal thickness in the macula.<sup>16–22</sup>

cpRNFL thickness should theoretically reflect global RNFL damage, because all RGC axons assemble in the ONH. By contrast, GCC analysis is currently limited to the macular area (6 × 6 mm square or circle of 6 mm in diameter). Thus, this method does not reflect loss of all RGCs, because only approximately 50% of RGCs are present within the macula, with the remainder outside the macula. Regardless of the limited area for macular GCC (mGCC) analysis, the glaucoma-discriminating ability of mGCC was reportedly comparable to that of cpRNFL.<sup>15–20</sup> However, we often see patients with early glaucoma who present RNFL defects outside the macular area. Thus, GCC analysis including an area wider than the macula may further improve glaucoma-discriminating ability.

Currently, only the RS3000 OCT device (Nidek, Gamagori, Japan), which enables the fastest image acquisition (53,000 A-scans/s), allows three-dimensional (3D) raster scanning (cube scan) over a 9 × 9 mm square region, providing a unique opportunity to investigate the glaucoma-discriminating ability of GCC in an area wider than the macula. The purpose of this study was to assess the glaucoma-discriminating ability of GCC thickness measured over a wider (8-mm diameter) area with 3D SD-OCT imaging.

From the Department of Ophthalmology and Visual Sciences, Kyoto University Graduate School of Medicine, Kyoto, Japan.

Supported in part by a Grant-in-Aid for Scientific Research (20592038) from the Japan Society for the Promotion of Science, Tokyo, Japan.

Submitted for publication March 17, 2012; revised May 28, 2012; accepted June 2, 2012.

Disclosure: **S. Morooka**, None; **M. Hangai**, Nidek (C), Topcon (C), Heidelberg Engineering (R), Santen (R); **M. Nukada**, None; **N. Nakano**, None; **K. Takayama**, None; **Y. Kimura**, None; **T. Akagi**, None; **H.O. Ikeda**, None; **A. Nonaka**, None; **N. Yoshimura**, Nidek (C), Heidelberg Engineering (R)

Corresponding author: Masanori Hangai, Department of Ophthalmology and Visual Sciences, Kyoto University Graduate School of Medicine, 54 Kawahara-cho, Shogoin, Sakyo-ku, Kyoto 606-8507, Japan; hangai@kuhp.kyoto-u.ac.jp.

## METHODS

### Patients

Study subjects who met the eligibility criteria and underwent examination by RS3000 were enrolled from a database of patients who were examined for glaucoma between September 2009 and July 2010 at the Department of Ophthalmology, Kyoto University Hospital. Candidates for the study included patients with either preperimetric glaucoma (PPG) or early glaucoma (EG) and volunteers without glaucoma who had at least one eye with a best corrected visual acuity of 20/20 or better in Snellen equivalent, spherical refractive error greater than  $-6.00$  diopters (D) and less than 3 D, a normal open anterior chamber angle, good quality of red-free photography, and reliable visual field tests. Subjects were assigned to the PPG, early EG, or normal control group. The PPG group demonstrated apparent glaucomatous optic disc appearance and normal standard automated perimetry (SAP) results. The EG group demonstrated apparent glaucomatous optic disc appearance associated with glaucomatous visual field defects with a mean deviation of greater than  $-6$  dB. Glaucomatous disc appearance was defined as diffuse or localized neuroretinal rim thinning evaluated on stereo color fundus photographs. Volunteer eyes were assigned to the healthy control group when they demonstrated normal optic disc appearance, no visible RNFL defect on red-free RNFL photography, an intraocular pressure of 21 mm Hg or lower with no history of increased IOP, and no family history of glaucoma in a first-degree relative. Data for candidate control eyes were retrospectively collected from our database of normal volunteers who were determined by our department to have at least one normal eye and who agreed to undergo the examinations described in this study. In cases in which both eyes of a subject were eligible for the study, only one eye was randomly chosen for inclusion.

Exclusion criteria for both groups were history of ocular surgery and evidence of vitreoretinal disease, uveitis, nonglaucomatous optic neuropathy or diabetes mellitus, or any other systemic disease that could affect the eye and visual field results. Patients for whom reliable OCT results could not be obtained were also excluded from the study. A total of 93 subjects including 46 healthy eyes of 46 volunteers and 47 eyes of 47 patients with glaucoma (23 eyes with PPG and 24 eyes with EG) were enrolled.

All patients underwent a comprehensive ophthalmic examination, including measurement of uncorrected and best-corrected visual acuity using the 5-meter Landolt chart, slit-lamp examinations, IOP measurements using a Goldman applanation tonometer, gonioscopy, dilated stereoscopic examination of the ONH, stereo disc photography with a 3-Dx simultaneous stereo disc camera (Nidek, Gamagori, Japan), red-free fundus photography using a Heidelberg Retina Angiogram 2 (HRA2, Heidelberg Engineering), SAP using a Humphrey Visual Field Analyzer (Carl Zeiss Meditec), and SD-OCT examination with the RS3000 system (Nidek).

All investigations in this study adhered to the tenets of the Declaration of Helsinki. This study was approved by the Institutional Review Board and Ethics Committee of the Kyoto University Graduate School of Medicine. Informed consent was obtained from the subjects after explanation of the nature and possible consequences of the study.

### Visual Field Testing

Reliable visual field results (fixation loss  $\leq 20\%$ , false-positive  $\leq 15\%$ , and false-negative  $\leq 33\%$ ) on SAP using the Humphrey 24-2 Swedish Interactive Threshold Algorithm (SITA) (HFA, Carl Zeiss-Meditec) were used. Abnormal visual field defects were defined using the 24-2 Swedish Interactive Threshold Algorithm standard program as (1) abnormal range on the glaucoma hemifield test; and (2) three abnormal points with  $P$  less than 5% probability of being normal, one abnormal point with  $P$  less than 1% by pattern deviation; or (3) pattern standard

deviation (PSD) of less than 5% of the normal reference, confirmed on two consecutive tests.

### Optic Disc Evaluation

The appearance of the optic nerve head on fundus photographs, including the stereoscopic photographs, was independently evaluated by three glaucoma specialists (M.H., H.O.I., and A.N.) who were masked to all other data about the eyes. Images of each eye from both healthy and PPG candidates were displayed on a monitor. If the decisions of all three examiners were not in agreement, consensus was reached by group review and discussion of the fundus color photographs and stereophotographs.

### Wide Area Three-Dimensional Spectral-Domain Optical Coherence Tomography Imaging

The RS-3000 system (software version 2.0.0) was used to perform 3D SD-OCT imaging. This instrument includes a confocal scanning laser ophthalmoscope to monitor fundus images and SD-OCT equipment to obtain tomographic images. The OCT equipment has a 5- $\mu$ m depth resolution in tissue and 20- $\mu$ m transverse resolution. Each A-scan of this instrument had a depth of 2 mm and comprised 512 pixels, providing a digital depth sampling of 3.9  $\mu$ m per pixel. For wide-area 3D imaging in the posterior pole, raster scanning over a 9  $\times$  9-mm square area centered on the foveal center was conducted with a scan density of 512 A-scans (horizontal)  $\times$  128 B-scans (vertical). For cpRNFL imaging, raster scanning over a 6  $\times$  6-mm square area centered on the optic disc center was conducted with a scan density of 512 A-scans (horizontal)  $\times$  128 B-scans (vertical). It took 1.6 seconds to obtain a single 3D data set. Imaging was performed by a well-trained examiner after pupillary dilatation, with the examiner rejecting any scans with motion artifacts (discontinuous jump), poor centration, incorrect segmentation, poor focus, or missing data and accepting only good-quality images, defined as those with "Signal Strength Index" scores (as assigned by the RS3000) of at least 6/10 (as suggested by the manufacturer).

### Measurements

Automated measurements of GCC and cpRNFL thickness were performed, and thickness and significance maps for GCC and cpRNFL thickness were generated using in-built software of the RS3000. The GCC thickness was measured between the internal limiting membrane and the outer boundary of the inner plexiform layer (IPL). cpRNFL thickness was measured in a circle 3.45 mm in diameter consisting of 256 A-scans, which were positioned automatically around the optic disc in each 3D data set.

### Wide Sector Chart

For this study, we used a modified glaucoma sector chart (GSC),<sup>21</sup> which was originally used by Wollstein et al.<sup>11</sup> to investigate the relationship between total macular thickness and visual field defects in eyes with glaucoma. The GSC was created by rotating the Early Treatment Diabetic Retinopathy Study (ETDRS) chart centered on the fovea by 45 degrees. The ETDRS chart was originally designed for evaluating diabetic macular edema and is not optimized for glaucoma detection. This chart includes four sectors that cross the horizontal meridian, which does not appear to reflect the anatomy of the RNFL. The GSC layout, which divides the macula by vertical and horizontal lines through the central fovea into superior, inferior, temporal, and nasal quadrants, better represented glaucomatous damages compared with the ETDRS.<sup>19</sup> Our wide macular sector chart based on the GSC layout divides the macula into inner, middle, and outer rings, with the inner ring 1 to 4 mm from the foveal center, the middle ring being from 4 to 6 mm from the foveal center, and the outer ring 6 to 8 mm from the foveal center (Fig. 1). Because the 8-mm circle sometimes overlaps

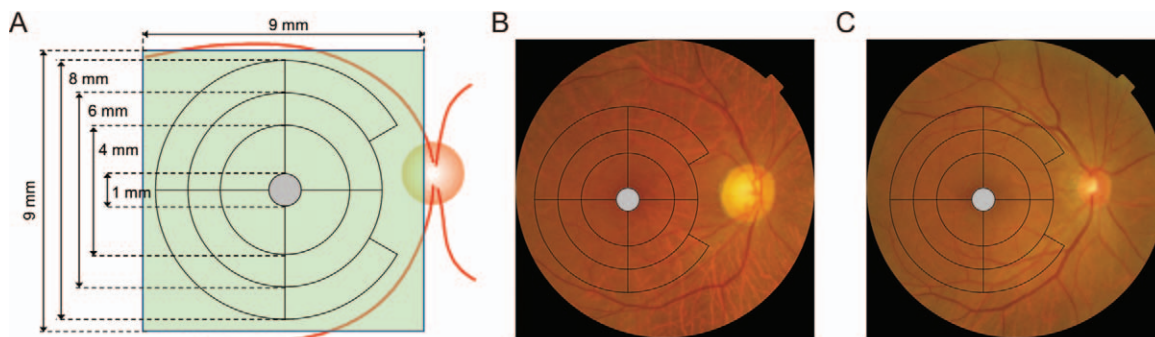


**FIGURE 1.** Schemata showing the wide sector chart for ganglion cell complex thickness. (A) *Light green square* shows the region for wide three-dimensional raster scanning. The wide sector chart consists of a circle 8 mm in diameter, divided by 1-mm, 4-mm, and 6-mm concentric circles into the inner, middle, and outer rings, and by vertical and horizontal lines through the central fovea into superior, inferior, temporal, and nasal quadrants. (B, C) Color fundus photographs with the wide sector chart overlain. Some eyes showed the arcade vessels not passing the outer ring as seen in (B), whereas others showed the arcade vessels passing the outer ring as seen in (C).

the optic disc, we removed the nasal part of the outer ring within 60 degrees (Fig. 1B).

**Statistical Analysis**

The statistical significance of differences in the continuous data between two groups was evaluated with the Mann-Whitney test and among three groups by ANOVA followed by post hoc test (Bonferroni). Levels of *P* less than  $0.05/3 = 0.0166$  were considered statistically significant for Bonferroni, and those of *P* less than 0.05 for other statistical analyses. To assess the ability of GCC thickness in various sectors to discriminate eyes with glaucoma from normal eyes, the area under the receiver operating characteristic curve (AROC) was calculated for each measurement. An AROC displays the relationship between sensitivity and 1 - specificity for the result of a given diagnostic test. An AROC of 1.0 indicates that the test perfectly discriminates between the presence or absence of the condition, whereas an AROC of 0.5 represents chance discrimination. Commercially available software (MedCalc version 9.3.8.0, Med Calc Software, Mariakerke, Belgium) was used to compare AROCs. The coefficient of variation (CV,  $100 \times SD/overall\ mean$ ) and intraclass correlation coefficient (ICC) were calculated from measurements obtained from three imaging sessions at the same visit.

**RESULTS**

**Subjects**

All of the enrolled subjects were Japanese. Subject demographics and visual field mean deviation (MD) of the three groups are shown in Table 1. No statistically significant differences in age, sex, or spherical equivalent of refractive errors were observed

among the three groups. Visual field MD values did significantly differ among the three groups.

**Case Showing Retinal Nerve Fiber Layer Defects Outside the Standard Sector Chart**

Figure 2 shows a case of PPG, in which abnormal thinning (<1% of confidence intervals of normative data base) of the GCC corresponding to a RNFL defect was detected in the wide sector chart but not in the standard sector chart. The color disc photograph shows localized thinning in the superotemporal neuroretinal rim associated with an RNFL defect. The red-free photograph shows a wedge-shaped localized RNFL defect near the superotemporal vascular arcade, which appears to be located outside the macula. The significance map of GCC thickness demonstrated a wedge-shaped arcuate area with red color (<1% outside the macula [standard chart [1-6-mm ring]). A large portion of the arcuate area was located within the outer ring (6-8 mm).

**Comparison of Ganglion Cell Complex and Circumpapillary Retinal Nerve Fiber Layer Thicknesses**

Average GCC thickness in the standard (1-6-mm ring) and wide (1-8-mm ring) sector charts and average cpRNFL thickness significantly differed among the three groups (Table 2). All thickness parameters were significantly smaller in the PPG and EG groups compared with the healthy control group, whereas no statistical differences in these parameters were observed between the PPG and EG groups.

**TABLE 1.** Subject Demographics

	Healthy	PPG	EG	<i>P</i> Value
Number	46	23	24	
Age, y				
Range	29-76	31-71	28-73	
Mean ± SD	54.6 ± 12.8	56.8 ± 9.4	51.9 ± 12.2	0.372*
Sex, male/female	21/25	7/16	11/13	0.436†
SE (D), Mean ± SD	-0.89 ± 1.94	-1.77 ± 2.48	-1.07 ± 2.25	0.282*
MD on SAP (dB), Mean ± SD	0.03 ± 1.26	-0.63 ± 1.10	-2.60 ± 1.47	<0.001*

SE, spherical equivalent refractive errors.

\* ANOVA.

† Chi-square test.

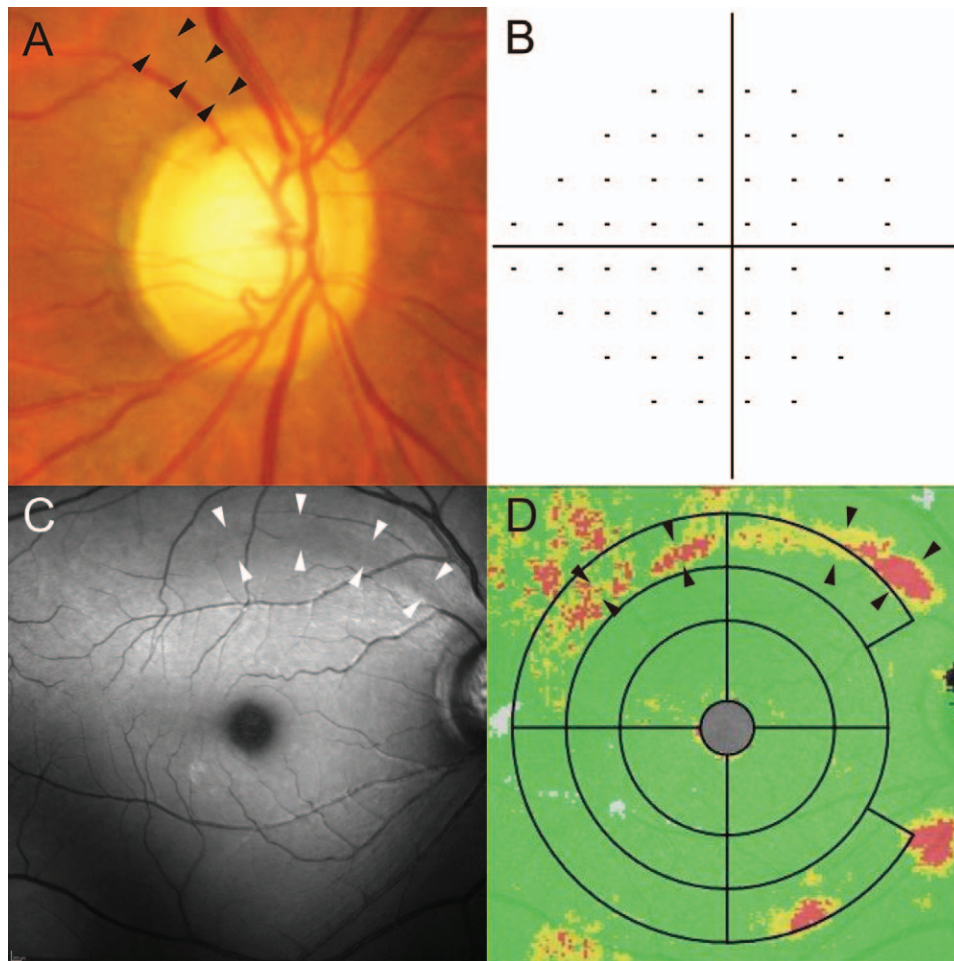


**FIGURE 2.** A case of retinal nerve fiber layer defect located outside the macula. The patient was a 74-year-old woman, and IOP in the right eye was 15 to 18 mm Hg without glaucoma medication. (A) Color disc photograph shows neuroretinal rim thinning in the superotemporal area associated with a narrow retinal nerve fiber layer (RNFL) defect (*arrowheads*). A small disc hemorrhage is seen on the rim temporal to the rim thinning. (B) Humphrey 24-2 SITA standard pattern deviation map. The mean deviation (MD) was  $-0.10$  dB. (C) A red-free fundus photograph shows wedge-shaped RNFL defect in the superotemporal sector (*arrowheads*). (D) Deviation-from-normal map shows wedge-shaped GCC thinning (*arrowheads*) corresponding to the RNFL defect on the red-free fundus photograph. *Red* = abnormal thinning (mean thickness less than the lower 99% confidence interval [CI] value in normal eyes). *Yellow* = borderline thinning (mean thickness between the lower 95% and lower 99% CI values in normal eyes). *Green* = within normal limits (mean thickness within the 95% CI in normal eyes).

**Comparison of Areas under Receiver Operating Characteristic Curves for Ganglion Cell Complex Thickness between Standard and Wide Sector Charts**

The AROCs for average GCC thickness in the wide chart (1–8-mm ring) were significantly greater than those of the standard

chart (1–6-mm ring) in eyes with PPG, EG, and both (Table 3, Fig. 3). The AROCs for average GCC thickness in the wide chart were more than 0.9 in eyes with PPG, EG, or both, whereas those of average cpRNFL thickness were less than 0.9 in eyes with PPG. The AROCs for average GCC thickness in the wide chart area and average cpRNFL thickness did not significantly differ in eyes with PPG, EG, or both.

**TABLE 2.** Comparison of Average Ganglion Cell Complex and Circumpapillary Retinal Nerve Fiber Layer Thicknesses between Standard and Wide Sector Charts

	Healthy	PPG	EG	P Value*	P1†	P2†	P3†
GCC (1–6 mm)	108.2 ± 5.5 (98.9–122.5)	96.0 ± 8.8 (73.3–109.1)	94.9 ± 10.8 (72.6–114.6)	<0.001	<0.001	<0.001	1.000
GCC (1–8 mm)	101.7 ± 5.3 (93.3–114.7)	88.2 ± 8.3 (70.7–100.3)	86.9 ± 9.5 (72.0–104.9)	<0.001	<0.001	<0.001	1.000
cpRNFL	104.8 ± 8.6 (82.6–127.0)	87.2 ± 7.8 (75.6–98.7)	87.0 ± 11.4 (71.4–110.2)	<0.001	<0.001	<0.001	1.000

Values are mean ± SD of thickness (μm) with ranges in parentheses.  
 P1, normal versus PPG; P2, normal versus EG; P3, PPG versus EG.  
 \* ANOVA.  
 † Post hoc test (Bonferroni).

TABLE 3. Comparison of AROCs for GCC Thickness in Standard Sector Chart (1-6-mm ring) and Wide Sector Chart (1-8-mm ring)

	GCC		P1	cpRNFL	P2
	1-8-mm Ring	1-6-mm Ring			
Healthy vs. PPG	0.928 (0.866-0.989)	0.891 (0.805-0.961)	0.038	0.874 (0.789-0.959)	0.154
Healthy vs. EG	0.912 (0.826-0.998)	0.861 (0.749-0.972)	0.003	0.888 (0.796-0.979)	0.315
Healthy vs. PPG+EG	0.920 (0.864-0.976)	0.876 (0.802-0.951)	0.004	0.881 (0.813-0.949)	0.373

AROCs with confidence intervals inside parentheses.  
 P1, 1-8-mm ring versus 1-6-mm ring; P2, 1-8-mm ring versus cpRNFL.

**Comparison of Areas under the Receiver Operating Characteristic Curves for Regional Average Ganglion Cell Complex Thickness in Wide Sector Chart**

To determine the diagnostic power of regional average GCC thickness in the wide sector chart, we compared AROCs in each sector between the middle ring (4-6 mm) and outer ring (6-8 mm). Overall, the AROCs of regional GCC thicknesses were nearly comparable; the middle and outer sectors statistically significantly differed only in the temporal inferior sector for eyes with PPG (Table 4).

**Measurement Variability and Reproducibility in Standard and Wide Sector Charts**

CVs were 0.68% and 0.97% in the standard and wide sector charts, respectively, in eyes with PPG, and 0.45% and 0.72% in the standard and wide sector charts, respectively, in eyes with EG. ICCs were 0.983 and 0.978 in the standard and wide sector charts, respectively, in eyes with PPG, and 0.998 and 0.994 in the standard and wide sector charts, respectively, in eyes with EG.

**Regional Measurement Variability and Reproducibility of the Wide Sector Chart**

The CVs and ICCs in all of the sectors in the wide sector chart are summarized in Table 5. The CVs in the outer ring (6-8 mm) tended to be greater compared with the inner ring (1-4 mm) and middle ring (4-6 mm); they are particularly large (>4.0) in the temporal inferior sectors of the outer ring. Low ICCs were observed in the temporal inferior (PPG and EG) and temporal superior sectors (PPG) in the outer ring, and the temporal superior sector in the middle ring (PPG). The ICCs in all other sectors were greater than 0.9.

**DISCUSSION**

Macular GCC thickness has been shown to be comparable and complementary to cpRNFL thickness in glaucoma-discriminating ability.<sup>16-20</sup> However, we do not need to limit the area for the measurement of GCC thickness to the macula (6 mm in diameter) for glaucoma diagnosis. In fact, we often see patients with RNFL defects outside the macula, as shown in Figure 2. However, the glaucoma-discriminating ability of GCC thickness outside the macula has not been previously reported. The current study demonstrated that, although variability was slightly greater and reproducibility somewhat worse outside the macula (outer ring [6-8 mm]), inclusion of the GCC thickness in the outer ring to the standard mGCC analysis significantly increased glaucoma-discriminating ability.

Anatomical characteristics of the GCL and RNFL may underlie this finding. The GCL thickness increases steeply as a function of distance from the central fovea, with a peak around 1 mm, and then gradually decreases with greater distance from the fovea<sup>14,22-25</sup>; this thickness pattern stems from the RGC density topographic pattern.<sup>26</sup> By contrast, RNFL thickness in the posterior pole is smallest around the fovea and gradually increases with greater distance from the fovea in the superior, nasal, and inferior regions.<sup>22-26</sup> Thus, the RNFL thickness appears to contribute to the diagnostic utility of GCC thickness, particularly in the extramacular region. In fact, circumpapillary RNFL thickness peaks in the superotemporal and inferotemporal regions, referred to as double humps.<sup>27-31</sup> The “double humps,” which are the arcuate bundles of the thickest RNFL and not just double humps, are reportedly located between 120° and 135° in the superotemporal and 270° and 285° in the inferotemporal region, a large part of which is located outside the macula (6-mm diameter circle).<sup>23,27-31</sup>

Recently, Garvin et al.<sup>32</sup> established a correlation map between RNFL thickness in peripapillary wedge sectors of superotemporal and inferotemporal quadrants (15 degrees in

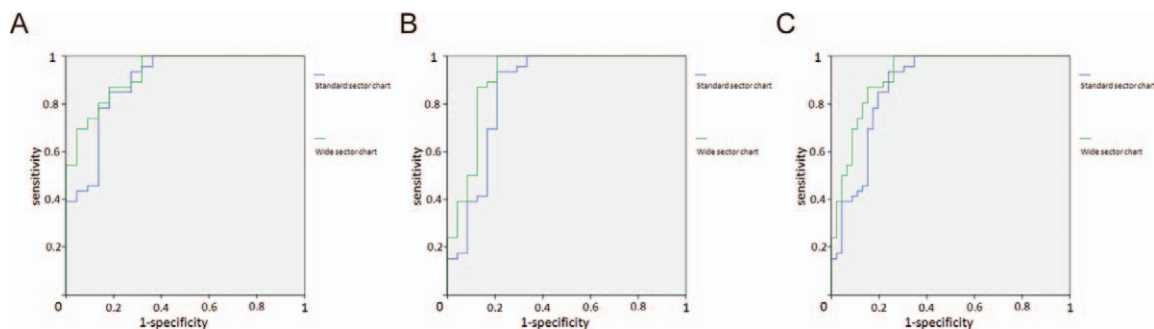


FIGURE 3. Receiver operating characteristic (ROC) curves for discriminating between healthy and glaucoma eyes at different stages. (A) Preperimetric glaucoma. (B) Early glaucoma. (C) All eyes. Blue and green lines indicate standard (1-6-mm ring) and wide (1-8-mm ring) sector charts, respectively.

TABLE 4. Comparison of AROCs for Regional Average GCC Thickness between Middle and Outer Sectors in Wide Sector Chart (1–8-mm Ring)

	Healthy vs. PPG			Healthy vs. EG			Healthy vs. PPG+EG		
	4–6 mm	6–8 mm	P1	4–6 mm	6–8 mm	P2	4–6 mm	6–8 mm	P3
Nasal inferior	0.863	0.874	0.789	0.783	0.815	0.436	0.822	0.844	0.543
Nasal superior	0.722	0.681	0.475	0.663	0.757	0.091	0.692	0.720	0.558
Temporal inferior	0.921	0.848	0.018	0.865	0.905	0.143	0.892	0.877	0.553
Temporal superior	0.826	0.757	0.092	0.740	0.794	0.143	0.782	0.776	0.864
Total	0.887	0.880	0.837	0.877	0.907	0.374	0.881	0.896	0.616

P1, Healthy control versus PPG; P2, Healthy control versus EG; P3, Healthy control versus PPG+EG.

each sector) and GCL thickness in macular grid regions as measured with SD-OCT in patients with glaucoma and suspected glaucoma. This map showed that the top-most or bottom-most two wedge sectors (corresponding to 30 degrees) had highest correlations with only a few superior or inferior macular peripheral grids. This structure-structure correlation model may support the validity of our hypothesis that the sampling on RGC axons outside the macular region en route to the optic disc enhances the glaucoma discriminating ability.

Lee et al.<sup>33</sup> reported that photographic RNFL defects were most commonly identified in the 7 and 11 o'clock sectors, and in some eyes in the 6 and 12 o'clock sectors, indicating that RNFL defects occur at variable locations and cannot all be detected by macular-area GCC analysis. Leung et al.<sup>34</sup> reported that 75% to 80% of glaucoma patients demonstrated tomographic RNFL loss evident at the inferotemporal meridians between 90° and 72°, with a peak at 76° as measured from the temporal horizontal line. Because RNFL at this angle assembles from almost outside the macula, it is possible that some regions outside the macula exist in which GCC thickness has high glaucoma-discriminating ability. In fact, in our study, the outer ring (6–8 mm) demonstrated comparable AROC values to the middle ring in eyes with preperimetric and early glaucoma. Thus, glaucomatous structural damages are often located outside the macula, which may be responsible for our finding that inclusion of the extramacular area to the standard mGCC thickness chart significantly increased glaucoma-discriminating ability.

The measurement variability in the outer ring (6–8 mm) and its sectors was relatively high compared with those of the middle (4–6 mm) and inner (1–4 mm) rings and their sectors. A possible reason for the higher measurement variability in the outer ring is that some eyes included larger blood vessels, such as the arcade vessels and their first branch vessels in the outer ring (Fig. 1C). Larger blood vessels likely interfere with the accuracy of boundary segmentation, consequently increasing the measurement variability of GCC. In general, high variability in thickness measures decreases AROC values. Another possible cause for measurement variability is the deviation from the preset scan pattern on the posterior pole due to involuntary ocular movements. This can occur because it took 1.6 seconds to obtain a single 3D data set. However, we discarded the images with apparent motion artifacts during OCT examination. Therefore, the effects of the deviations would be minimal. Moreover, it is uncertain whether the effects of the deviations are largest particularly in the outer ring because the changes in the GCC thickness as a function from the fovea are rather largest in the inner ring.

Regardless of the higher measurement variability in the outer ring compared with those in the middle and inner rings, the addition of the outer ring (wide sector chart [1–8 mm]) to the standard sector chart (1–6 mm) significantly increased the AROCs, and the AROCs of the outer ring were comparable to those of the middle ring in eyes with EG and PPG. The reason for these seemingly contradictory results is uncertain. One possibility is that the outer ring (6–8 mm) can cover the RNFL over a wider area compared with middle and inner rings. The

TABLE 5. Regional Measurement Variability and Reproducibility

	%CVs of Repeated Measures			ICCs of Repeated Measures		
	1–4 mm	4–6 mm	6–8 mm	1–4 mm	4–6 mm	6–8 mm
Nasal inferior						
PPG	0.55	1.89	2.03	0.984	0.911	0.966
EG	0.91	1.51	3.26	0.995	0.976	0.927
Nasal superior						
PPG	0.49	0.42	1.90	0.978	0.997	0.977
EG	0.50	0.67	2.67	0.998	0.997	0.957
Temporal inferior						
PPG	1.07	3.09	5.37	0.992	0.932	0.652
EG	0.74	1.55	4.85	0.998	0.979	0.530
Temporal superior						
PPG	0.84	1.95	3.88	0.984	0.702	0.753
EG	0.79	1.06	1.60	0.995	0.994	0.966
Total						
PPG	0.48	1.44	2.25	0.993	0.849	0.920
EG	0.54	0.85	1.88	0.997	0.986	0.934

retinal nerve fibers that pass the macula (= middle ring + inner ring) also pass the outer ring, whereas those that pass the outer ring do not necessarily pass the middle or inner rings.

The RS3000, which currently enables the fastest image acquisition (53,000 A-scans/s), allows 3D raster scanning (cube scan) over a  $9 \times 9$ -mm square region in 1.6 seconds. However, we did not use the 8- to 9-mm ring area for this analysis, first, because the GCC measurements in sectors of this ring demonstrated high variability (%CV, 1.64%–7.36%, data not shown). This variability is probably attributable to the inclusion of larger vessels, which could increase the measurement variability, as already mentioned.<sup>35</sup> In addition, the 9-mm circle includes a larger part of the optic disc (Fig. 2), where the GCC cannot be measured. We also did not use the 8- to 9-mm ring area because the 3D raster-scan protocol bounded by the  $9 \times 9$ -mm square does not actually cover the entire region of the 9-mm circle chart area for measurement, when the central points of the  $9 \times 9$ -mm square scan area and the 9-mm circle area do not match exactly. In such cases, the thickness of the peripheral areas of the 8- to 9-mm ring area that was outside the  $9 \times 9$ -mm square cannot be measured.

In our study, the average GCC thickness in the standard (1–6 mm) or wide (1–8 mm) sector chart did not have significantly higher AROCs compared with cpRNFL. Although the AROC to distinguish between healthy and PPG eyes for cpRNFL thickness was even smaller than that for GCC thickness in the standard sector chart, no significant difference was found for AROCs between cpRNFL thickness and GCC thickness in the wide sector chart. This is probably attributable to the relatively large confidence intervals of the AROCs for cpRNFL. Our result is consistent with previous studies<sup>16–20</sup> and has been attributed to the anatomical characteristics of mGCC and cpRNFL. A cpRNFL scan samples nearly all axons arising from RGCs, whereas an mGCC scan covers only the macular area. However, the mGCC scan samples macular damage better than the cpRNFL scan because the GCC includes the GCL, and it may be able to more sensitively detect glaucomatous changes where macular loss occurs early or predominantly. Even if the measurement area is enlarged from a 6-mm to 8-mm circle, the anatomical relationship between cpRNFL and GCC remains.

A limitation of this study is that we tested only one in-built segmentation algorithm of the RS3000 instrument. Measurement variability was relatively high in the extramacular area compared with macular areas, and in the temporal inferior area compared with other areas. The latter may be attributable to the smaller thickness of the GCC as a result of glaucomatous damage. The inferotemporal area is the most frequent to suffer from glaucomatous damages.<sup>16,21</sup> The accuracy and variability of GCC segmentation in these areas depends most on segmentation algorithm. Reducing the variability of segmentation in these areas could further improve glaucoma-discriminating ability.

Regardless of these limitations, our study successfully demonstrated that addition of extramacular GCC measurements to standard macular GCC analysis improved glaucoma-discriminating ability. Currently, widening of the 3D raster scan area is limited by the imaging speed of SD-OCT. As OCT technology advances in imaging speed, our findings may become more useful for enhancing the applicability of GCC analysis for glaucoma diagnosis.

## References

1. Quigley HA, Addicks EM, Green WR. Optic nerve damage in human glaucoma. III. Quantitative correlation of nerve fiber loss and visual field defect in glaucoma, ischemic neuropathy, papilledema, and toxic neuropathy. *Arch Ophthalmol*. 1982; 100:135–146.
2. Quigley HA, Dunkelberger GR, Green WR. Retinal ganglion cell atrophy correlated with automated perimetry in human eyes with glaucoma. *Am J Ophthalmol*. 1989;107:453–464.
3. Mardin CY, Jünemann AG. The diagnostic value of optic nerve imaging in early glaucoma. *Curr Opin Ophthalmol*. 2001;12: 100–104.
4. Townsend KA, Wollstein G, Schuman JS. Imaging of the retinal nerve fibre layer for glaucoma. *Br J Ophthalmol*. 2009;93:139–143.
5. Zeimer R, Asrani S, Zou S, Quigley H, Jampel H. Quantitative detection of glaucomatous damage at the posterior pole by retinal thickness mapping. *Ophthalmology*. 1998;105:224–231.
6. Trick GL, Calotti FY, Skarf B. Advances in imaging of the optic disc and retinal nerve fiber layer. *J Neuroophthalmol*. 2006; 26:284–295.
7. Giovannini A, Amato G, Mariotti C. The macular thickness and volume in glaucoma: an analysis in normal and glaucomatous eyes using OCT. *Acta Ophthalmol Scand Suppl*. 2002;236:34–36.
8. Guedes V, Schuman JS, Hertzmark E, et al. Optical coherence tomography measurement of macular and nerve fiber layer thickness in normal and glaucomatous human eyes. *Ophthalmology*. 2003;110:177–189.
9. Lederer DE, Schuman JS, Hertzmark E, et al. Analysis of macular volume in normal and glaucomatous eyes using optical coherence tomography. *Am J Ophthalmol*. 2003;135: 838–843.
10. Greenfield DS, Bagga H, Knighton RW. Macular thickness changes in glaucomatous optic neuropathy detected using optical coherence tomography. *Arch Ophthalmol*. 2003;121: 41–46.
11. Wollstein G, Schuman JS, Price LL, et al. Optical coherence tomography (OCT) macular and peripapillary retinal nerve fiber layer measurements and automated visual fields. *Am J Ophthalmol*. 2004;138:218–225.
12. Medeiros FA, Zangwill LM, Bowd C, Vessani RM, Susanna R Jr, Weinreb RN. Evaluation of retinal nerve fiber layer, optic nerve head, and macular thickness measurements for glaucoma detection using optical coherence tomography. *Am J Ophthalmol*. 2005;139:44–55.
13. Leung CK, Chan WM, Yung WH, et al. Comparison of macular and peripapillary measurements for the detection of glaucoma: an optical coherence tomography study. *Ophthalmology*. 2005;112:391–400.
14. Ishikawa H, Stein DM, Wollstein G, Beaton S, Fujimoto JG, Schuman JS. Macular segmentation with optical coherence tomography. *Invest Ophthalmol Vis Sci*. 2005;46:2012–2017.
15. Ojima T, Tanabe T, Hangai M, Yu S, Morishita S, Yoshimura N. Measurement of retinal nerve fiber layer thickness and macular volume for glaucoma detection using optical coherence tomography. *Jpn J Ophthalmol*. 2007;51:197–203.
16. Tan O, Chopra V, Lu AT, et al. Detection of macular ganglion cell loss in glaucoma by Fourier-domain optical coherence tomography. *Ophthalmology*. 2009;116:2305–2314.
17. Jeoung JW, Park KH. Comparison of Cirrus OCT and Stratus OCT on the ability to detect localized retinal nerve fiber layer defects in preperimetric glaucoma. *Invest Ophthalmol Vis Sci*. 2010;51:938–945.
18. Rao HL, Zangwill LM, Weinreb RN, Sample PA, Alencar LM, Medeiros FA. Comparison of different spectral domain optical coherence tomography scanning areas for glaucoma diagnosis. *Ophthalmology*. 2010;117:1692–1699e1.
19. Mori S, Hangai M, Sakamoto A, Yoshimura N. Spectral-domain optical coherence tomography measurement of macular volume for diagnosing glaucoma. *J Glaucoma*. 2010;19:528–534.

20. Rolle T, Briamonte C, Curto D, Grignolo FM. Ganglion cell complex and retinal nerve fiber layer measured by fourier-domain optical coherence tomography for early detection of structural damage in patients with preperimetric glaucoma. *Clin Ophthalmol*. 2011;5:961-969.
21. Kotera Y, Hangai M, Hirose F, Mori S, Yoshimura N. Three-dimensional imaging of macular inner structures in glaucoma by using spectral-domain optical coherence tomography. *Invest Ophthalmol Vis Sci*. 2011;52:1412-1421.
22. Nakano N, Hangai M, Nakanishi H, et al. Macular ganglion cell layer imaging in preperimetric glaucoma with speckle noise-reduced spectral domain optical coherence tomography. *Ophthalmology*. 2011;118:2414-2426.
23. Ooto S, Hangai M, Tomidokoro A, et al. Effects of age, sex, and axial length on the three-dimensional profile of normal macular layer structures. *Invest Ophthalmol Vis Sci*. 2011;52:8769-8779.
24. Curcio CA, Messinger JD, Sloan KR, Mitra A, McGwin G, Spaide RF. Human chorioretinal layer thicknesses measured in macula-wide, high-resolution histologic sections. *Invest Ophthalmol Vis Sci*. 2011;52:3943-3954.
25. Loduca AL, Zhang C, Zelkha R, Shahidi M. Thickness mapping of retinal layers by spectral-domain optical coherence tomography. *Am J Ophthalmol*. 2010;150:849-855.
26. Curcio CA, Allen KA. Topography of ganglion cells in human retina. *J Comp Neurol*. 1990;300:5-25.
27. Dichtl A, Jonas JB, Naumann GO. Retinal nerve fiber layer thickness in human eyes. *Graefes Arch Clin Exp Ophthalmol*. 1999;237:474-479.
28. Blumenthal EZ. Quantifying retinal nerve fiber layer thickness histologically: a novel approach to sectioning of the retina. *Invest Ophthalmol Vis Sci*. 2004;45:1404-1409.
29. Cohen MJ, Kaliner E, Frenkel S, Kogan M, Miron H, Blumenthal EZ. Morphometric analysis of human peripapillary retinal nerve fiber layer thickness. *Invest Ophthalmol Vis Sci*. 2008;49:941-944.
30. Essock EA, Sinai MJ, Bowd C, Zangwill LM, Weinreb RN. Fourier analysis of optical coherence tomography and scanning laser polarimetry retinal nerve fiber layer measurements in the diagnosis of glaucoma. *Arch Ophthalmol*. 2003;121:1238-1245.
31. Leung CK, Chan WM, Yung WH, et al. Comparison of macular and peripapillary measurements for the detection of glaucoma: an optical coherence tomography study. *Ophthalmology*. 2005;112:391-400.
32. Garvin MK, Abramoff MD, Lee K, Niemeijer M, Sonka M, Kwon YH. 2-D pattern of nerve fiber bundles in glaucoma emerging from spectral-domain optical coherence tomography. *Invest Ophthalmol Vis Sci*. 2012;53:483-489.
33. Lee EJ, Kim TW, Weinreb RN, Park KH, Kim SH, Kim DM. Trend-based analysis of retinal nerve fiber layer thickness measured by optical coherence tomography in eyes with localized nerve fiber layer defects. *Invest Ophthalmol Vis Sci*. 2011;52:1138-1144.
34. Leung CK, Choi N, Weinreb RN, et al. Retinal nerve fiber layer imaging with spectral-domain optical coherence tomography. *Ophthalmology*. 2010;117:2337-2344.
35. Golzan SM, Avolio A, Graham SL. Minimising retinal vessel artefacts in optical coherence tomography images. *Comput Methods Programs Biomed*. 2011;104:206-211.